ADVANCED OPTICAL MATERIALS
www.advopticalmat.de

A Universal Assembly Strategy of All-Inorganic Non-Layered Perovskite Single Crystals for High-Responsivity Photodetectors

Enliu Hong, Ziqing Li, Fa Cao, Xiaolei Deng, Xinyu Zhang, and Xiaosheng Fang**

Non-layered all-inorganic perovskite single crystals (AIPSCs) have ultralow trap density and exceptional optoelectronic properties, which can be used for developing high-performance perovskite optoelectronic devices with high efficiency and stability. However, there is a lack of comprehensive insight and universal principles to guide the preparation of high-quality AIPSCs. Herein, a universal liquid–air interfacial assembly strategy is proposed for synthesizing non-layered AIPSCs, in virtue of which a series of AIPSCs including whole structural dimensions from 0D to 3D are acquired. Specially, the $CsPbI_3$ AIPSCs exhibit an ultrathin thickness of 40 nm, and the $CsPbBr_3$ AIPSCs show ultra-narrow PL FWHM of 11 nm. Photodetectors (PDs) based on $CsPbBr_3$ show excellent performance with responsivity up to 120 A W^{-1} and detectivity exceeding 2×10^{13} Jones. Moreover, vertically integrated heterojunctions of mixed-dimensions are fabricated, and the 2D/3D heterostructure PDs further display enhanced self-powered characteristics. This work provides general synthetic guidance toward the synthesis of non-layered AIPSCs and promotes their application in AIPSCs-based optoelectronics.

1. Introduction

Perovskite single crystals (PSCs) have attracted tremendous attentions owning to their improved optoelectronic properties compared to polycrystalline counterparts, such as ultra-low trap densities, higher carriers mobilities, longer carrier lifetime, and diffusion lengths,[1–3] and so on, which are considered to be the state-of-art materials for the next-generation of optoelectronic devices. Meanwhile, all-inorganic perovskite single crystals (AIPSCs) possess better thermal stability, faster carrier transport and higher tolerance to moisture and oxygen than all-organic or organic–inorganic hybrid perovskites.[4,5] With the aim of improving the stability and reliability of perovskites-based devices, replacing the long-chain organic A-site cations by Cs^+ has been intensively investigated. And resultantly, the cesium-based AIPSCs have already been widely used in solar cells,[6] light-emitting diodes,[7] lasers,[8] photodetectors,[9] etc., due to their natural structural superiorities. Up to date, the preparation methods of PSCs mainly include conventional solution temperature lowering (STL), inverse temperature crystallization (ITC), antisolvent vapor-assisted crystallization (AVC), top-seeded solution growth (TSSG), chemical/physical vapor deposition (CVD/PVD), space-confined method,[10–12] and so on, each of which varies a lot in terms of treating processes and applicative targets. For instance, Fang et al. reported a room-temperature liquid diffused separation induced crystallization method for high-quality PSCs,[13] in which the artful density-dependent relationship of solvents is hard to be extended to inorganic systems. Moreover, this strategy is only applicable to prepare bulk PSCs and usually needs several days to complete the crystallization process because of the slow growth rate. As for ITC method,[14] toxic and easily volatile organic solvents are commonly used, which are harmful to experimental operators and environment. Besides, the temperature down rate and solvent volatilization speed need to be precisely controlled in the ITC process. For AVC crystallization, the sealing degree of the reaction system requires to be high.[15] In a word, the methods previously reported seem to be successful when applied to synthesize a single kind of target PSCs, whereas there is still a lack of a universal strategy to guide the preparation of diverse-dimensional PSCs, let alone non-layered AIPSCs. Therefore, developing a universal strategy and establishing its corresponding growth kinetics model holds great promise to obtain AIPSCs facilely and efficiently in the development of optoelectronic fields.

Benefiting from the solution-processability of perovskite materials, novel solution-based bottom-up self-assembly techniques of nanoparticles into nano-microstructures are emerging,[16–18] among which the interface (Liquid–liquid, liquid–air, liquid–solid) engineering is the most remarkable. In principle,

E. Hong, F. Cao, X. Deng, X. Zhang, X. Fang
Department of Materials Science
State Key Laboratory of Molecular Engineering of Polymers
Fudan University
Shanghai 200433, P. R. China
E-mail: xshfang@fudan.edu.cn
Z. Li, X. Fang
Shanghai Frontiers Science Research Base of Intelligent Optoelectronics and Perception
Institute of Optoelectronics
Fudan University
Shanghai 200433, P. R. China
E-mail: lzq@fudan.edu.cn

The ORCID identification number(s) for the author(s) of this article can be found under https://doi.org/10.1002/adom.202301182

DOI: 10.1002/adom.202301182

nanoparticles are induced to form high-quality PSCs through interfacial interaction, such as surface tension, electrostatic attraction, capillary effect, van der Waals force, etc.[19–22] Herein, we developed a universal assembly strategy for preparing nonlayered AIPSCs with whole structural dimensions at the liquid–air interface via the promotion of surface tension. Liquid–air interfacial assembly, which has been reported for the growth of 2D layered Ruddlesden–Popper (RP) hybrid lead halide PSCs,[23] but has never been applied to synthesize AIPSCs. This is probably because it's generally believed that the existence of organic hydrophobic alkylamine groups is an indispensable factor enabling the PSCs to grow free-standing and steadily at the interface. In this regard, we modified this method theoretically, proposed a new growth kinetics model and concluded a universal assembly strategy, then achieved surprising success experimentally. Utilizing this universal strategy, a series of AIPSCs with crystal structures ranging from 0D to 3D were obtained, including $Cs_3Bi_2I_9$ (CBI, 0D), $CsPbI_3$ (CPI, 1D), $Cs_3Sb_2I_9$ (CSI, 2D), $Cs_3Bi_2Br_9$ (CBB, 2D), $CsPbBr_3$ (CPB, 3D), and a lead-free double perovskite $Cs_2AgBiBr_6$ (CABB, 3D). In particular, low-dimensional CPI AIPSCs exhibit ultrathin thickness down to 40 nm and lateral size up to 200 μm. Compared to conventional synthesizing methods, the feature of this strategy is to fully utilize the solution-processability of perovskites. Different from commonly used organic solvents such as *N,N*-dimethylformamide (DMF), dimethyl sulfoxide (DMSO) and γ-butyrolactone (GBL), which are highly volatile and harmful to environment, our aqueous synthesis routine adopting green solvent (water medium) is more suitable for preparing AIPSCs with better moisture resistance. The cost is greatly reduced by adopting this minimalist preparation process, meanwhile, the excellent device performance could be guaranteed due to the high quality of the as-prepared AIPSCs.

2. Results and Discussion

The schematic illustration of interfacial assembly process of AIPSCs is shown in **Figure 1**a. Briefly, the surface-layer cations are subjected to asymmetric forces, initiating nucleation and crystal growth. Then buoyancy enables the AIPSCs to float at the liquid–air interface, while surface tension induces the AIPSCs to grow up. The size-time dependent relationship is shown in Figure 1b, it can be observed that the size of AIPSCs gradually increases over time as expected. As shown in Figure 1d, the surface of a liquid is like an elastic membrane, which could be strained to a certain degree. Once the liquid is under surface tension, it tends to keep its free surface area to the minimum to possess the lowest surface energy. As a result, the AIPSCs floating at the liquid surface are subjected to a lateral surface tension, promoting it to grow laterally.

The crystallization kinetics model of this interfacial growth phenomenon is established by involving the classical nucleation theory, according to which the relationship between the nucleation rate (I_v) and activation energy of solute molecules (ΔG_m) can be described as follows:

$$I_v = A \exp\left(-\Delta G_m / RT\right) \tag{1}$$

$$\Delta G_m = E_A - E_S \tag{2}$$

where A is a constant, R is molar gas constant, T is temperature, E_A and E_S represent the activated-state energy and surface free energy, respectively. The Gibbs–Wulff theorem shows that crystals growth follows the principle of minimum surface energy during the nucleation process, which means crystal prefers to grow up along the plane who owns lower surface energy. Generally speaking, the exposed surfaces outside the crystal are always the planes with the lowest surface energy.[24] Assume the surface energy vertical and parallel to the plane of crystal as E_{S1} and E_{S2} shown in Figure 1c (E_0 represents steady-state energy, λ represents the ion migration distance from liquid to crystalline phase and is approximately the interface thickness), the upper plane exposed at the liquid-air interface has lower surface energy than the side plane, i.e., $E_{S1} < E_{S2}$. Based on Equations (1) and (2), the anisotropic growth rate ratio α ($\alpha = I_{v1}/I_{v2}$) that determines the crystal morphology can be inferred as:

$$\alpha = \exp\left[\left(E_{S1} - E_{S2}\right)/\mathrm{RT}\right] \tag{3}$$

Obviously $\alpha < 1$, because $E_{S1} < E_{S2}$. In other words, the single crystals existing at the liquid–air interface prefer to grow up laterally. To grow PSCs down to the monolayer limit, α should be as small as possible, which means $E_{S1} \ll E_{S2}$. Note that for AIPSCs with 3D structure, surface tension is limited and insufficient to counteract gravity during growth process, so they easily sink to the bottom and hard to grow up steadily. In this regard, this universal assembly strategy could be applied to synthesize AIPSCs of diverse dimensions while it's more suitable for the growth of low-dimensional AIPSCs.

Experimentally, the universal growth results of AIPSCs with diverse structural dimensions and their corresponding photoluminescence (PL) spectra are presented in **Figure 2** and Figure S1 (Supporting Information). It can be seen that the as-grown AIPSCs varies a lot in morphology and size, with structural dimension span from 0D to 3D, both of which shows well-defined boundaries and characteristic shapes, thus validating the universality of our growth mechanism. Note that dimensional definition here refers to structural rather than morphological dimension. The PL feature peak positions of these AIPSCs are 684, 549, 435, 676, 758, and 672 nm for CPI, CPB, CBB, CBI, CSI, and CABB, respectively, which are well consistent with previous reports and confirm the crystals compositions.[25–30] Moreover, the PL spectra show sharp and strong peaks, illustrating the high crystallinity of these AIPSCs with few defects and trap density. Besides, there is also a big difference in the full width at half maximum (FWHM), which could reflect the crystalline quality.[31] Impressively, the CPB AIPSCs exhibit much narrower FWHM of 11 nm, indicating their much higher crystallinity with less nonradiative recombination and lower carrier scattering. And the differences in peak positions and FWHM also indicate the bandgap variety of these AIPSCs, which can be easily modulated by elements doping or composition engineering.[32] The height profile data in Figure S2 (Supporting Information) reveals the thickness of these AIPSCs. In particular, the 1D CPI nanobelts and 2D CSI nanosheets exhibit ultrathin thicknesses of 40 and 150 nm, respectively. The achieved preparation of AIPSCs has great significance in developing nanoscale optoelectronic applications,[33–35] which remains intriguing to be investigated. The growth results

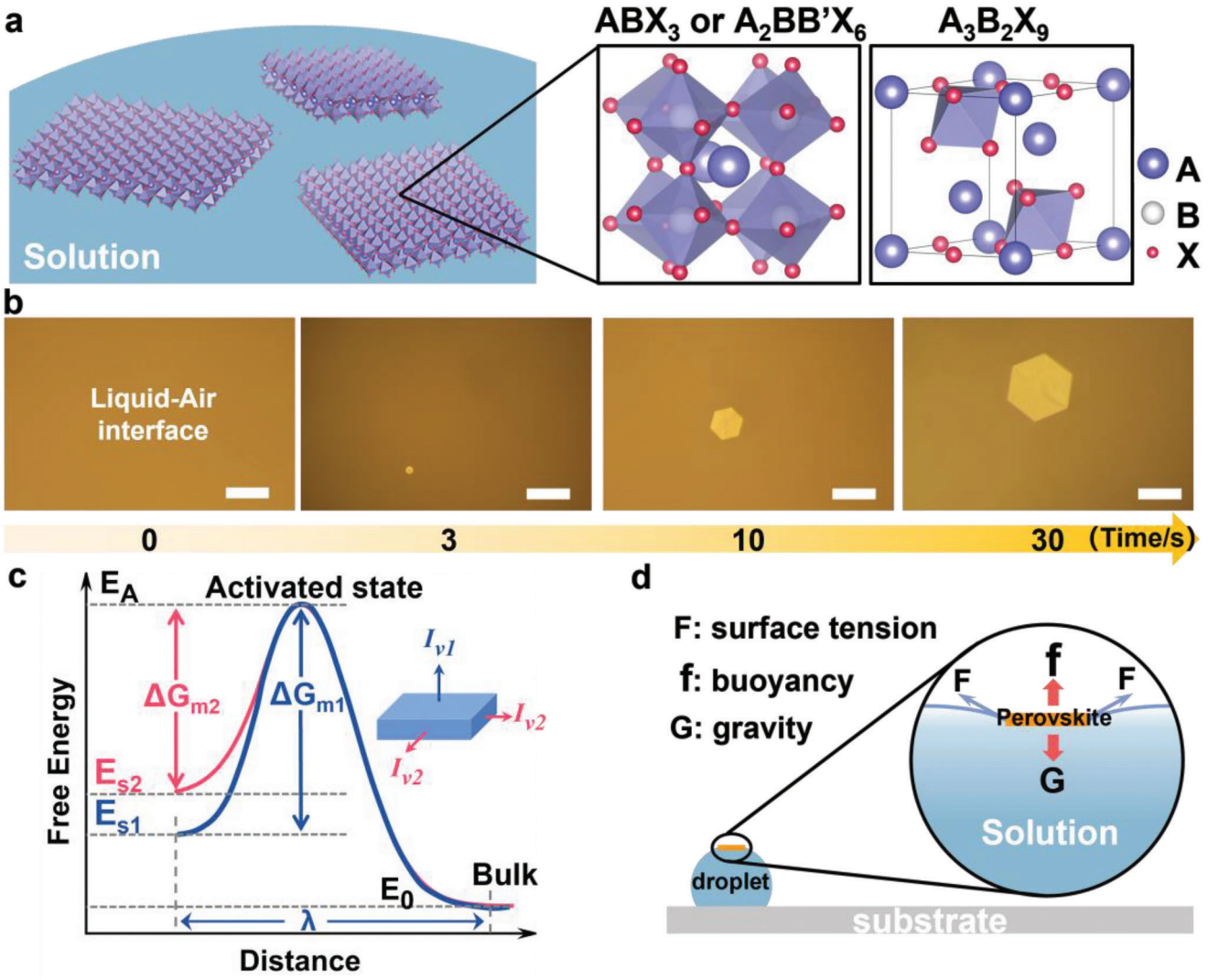

Figure 1. a) Scheme for the freestanding growth of ABX_3 AIPSCs at the liquid-air interface (A: Cs^+; B: Ag^+, Pb^{2+}, Sb^{3+}, Bi^{3+}; X: Br^-, I^-). b) Real-time growth observation of $Cs_3Sb_2I_9$ PSCs. (Scale bar: 50 μm). c) The Gibbs free energy change at different states. d) Force analysis diagram of AIPSCs staying afloat on the solution surface.

of these representative AIPSCs provide reliable evidence for the great universality of our strategy.

In order to further confirm the high crystallinity and chemical constitution of as-prepared AIPSCs, high-resolution transmission electron microscope (HRTEM), X-ray photoelectron spectroscopy (XPS), scanning electron microscope (SEM), and energy dispersive spectroscopy (EDS) mapping analysis were performed in representative CSI and CBI AIPSCs. HRTEM image of the CSI edge area exhibits clearly visible lattice stripes and the interlayer spacing of 0.29 nm is corresponding to the d spacing of (202) crystal planes (**Figure 3**a). The inverse fast Fourier transform (FFT) pattern (inset of Figure 3a) also shows the single crystal property of the CSI nanosheet with bright and periodic diffraction spots. The chemical composition of CSI nanosheets is verified by XPS spectra in Figure 3b and EDS mappings in Figure 3c, from which it can be seen that the elements of the constitution are Cs, Sb, I. As shown in Figure 3c and Figure S3 (Supporting Information), the SEM images of CSI and CBI both show good hexagonal morphology with clean and smooth surfaces. Meanwhile, their corresponding EDS mapping images reveal that the elemental distribution of CSI and CBI are very uniform, suggesting the high quality of our as-synthesized AIPSCs. The resulting stoichiometric ratio of Cs:Sb:I and Cs:Bi:I (Figure S4, Supporting Information), as calculated from the EDS analysis, are found to be 3.07:2.01:9.23 and 3.09:1.99:8.87, respectively, which agree well with the theoretical value of 3:2:9, further verified the composition.

It's generally acknowledged that 2D materials could serve as perfect support materials to combine with other components on account of their unique planar atomic structure and large specific surface area.[36] As shown in **Figure 4**a, the optical image and its PL mapping result of the same color of the selective region means the surface photoluminescence intensity are basically consistent, indicating the uniformity and high quality of our as-grown crystals. In other words, they are perfect to serve as bottom support materials to construct heterostructures. Thus,

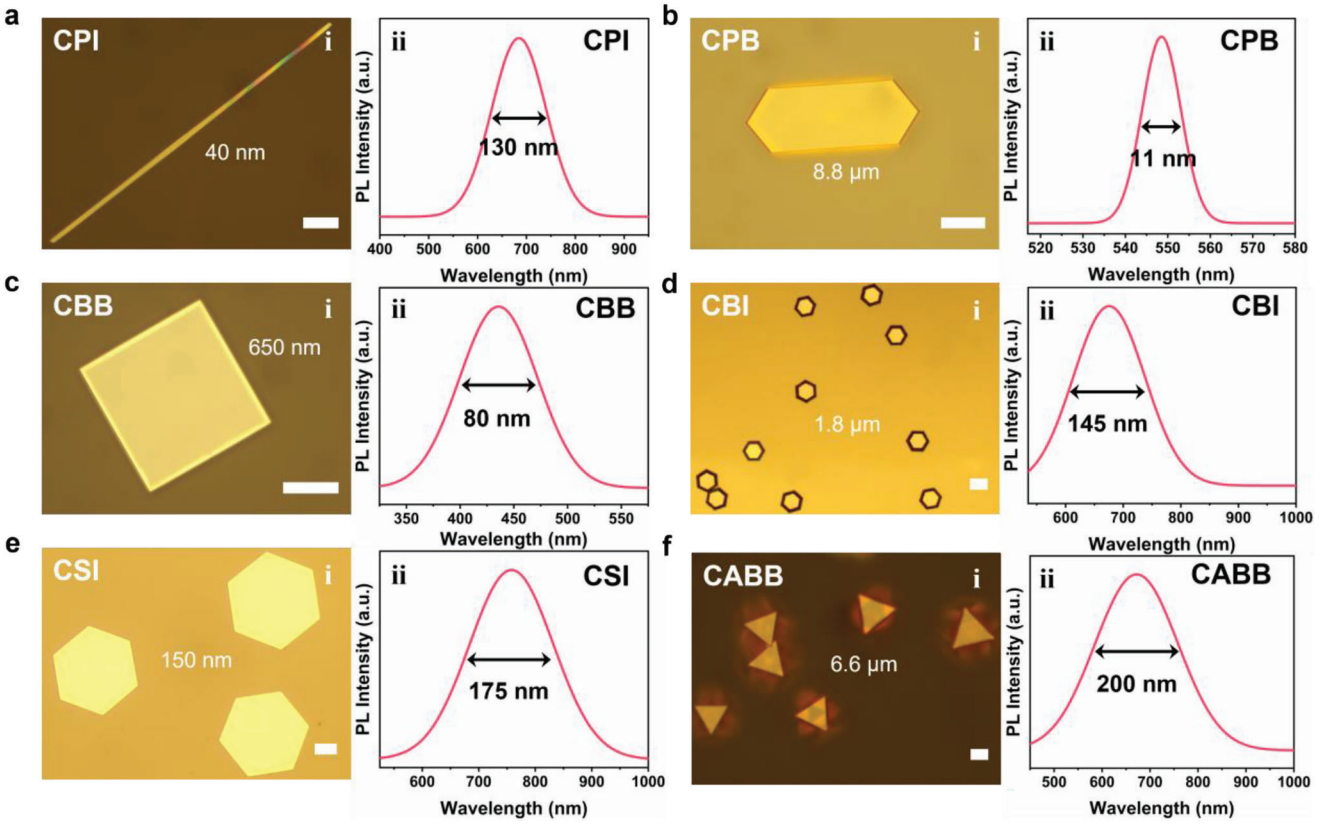

Figure 2. The universal growth of various dimensional AIPSCs. Optical microscope images of as-grown AIPSCs with different thickness and their corresponding PL spectra (λ_{ex} = 325 or 532 nm), scale bar: 20 μm. Dimensional definition here refers to structural rather than morphological dimension. a) 1D $CsPbI_3$ nanobelt, abbreviated as CPI. b) 3D $CsPbBr_3$ single crystal, abbreviated as CPB. c) 2D $Cs_3Bi_2Br_9$ nanoplate, abbreviated as CBB. d) 0D $Cs_3Bi_2I_9$, abbreviated as CBI. e) 2D $Cs_3Sb_2I_9$ nanosheet, abbreviated as CSI. f) 3D $Cs_2AgBiBr_6$ single crystal, abbreviated as CABB.

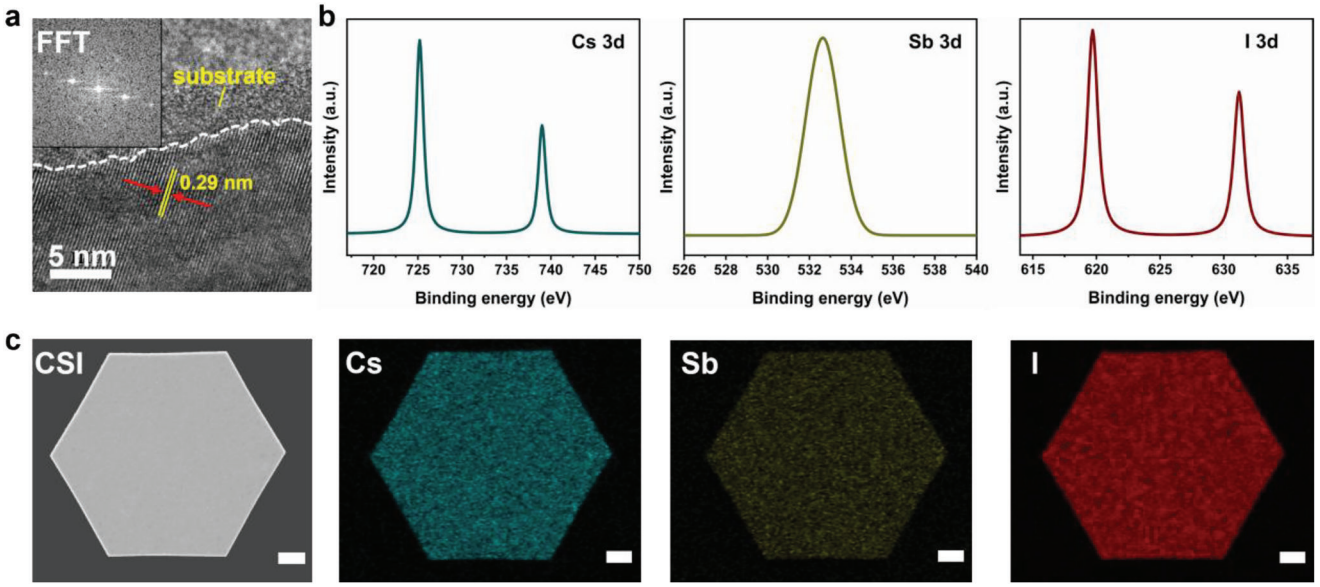

Figure 3. Structural characterization of the representative CSI AIPSCs. a) HRTEM image and corresponding FFT pattern (inset) of a CSI nanosheet. b) XPS Cs, Sb and I spectra. c) SEM image and its corresponding EDS mappings of a CSI nanosheet. Scale bar: 10 μm.

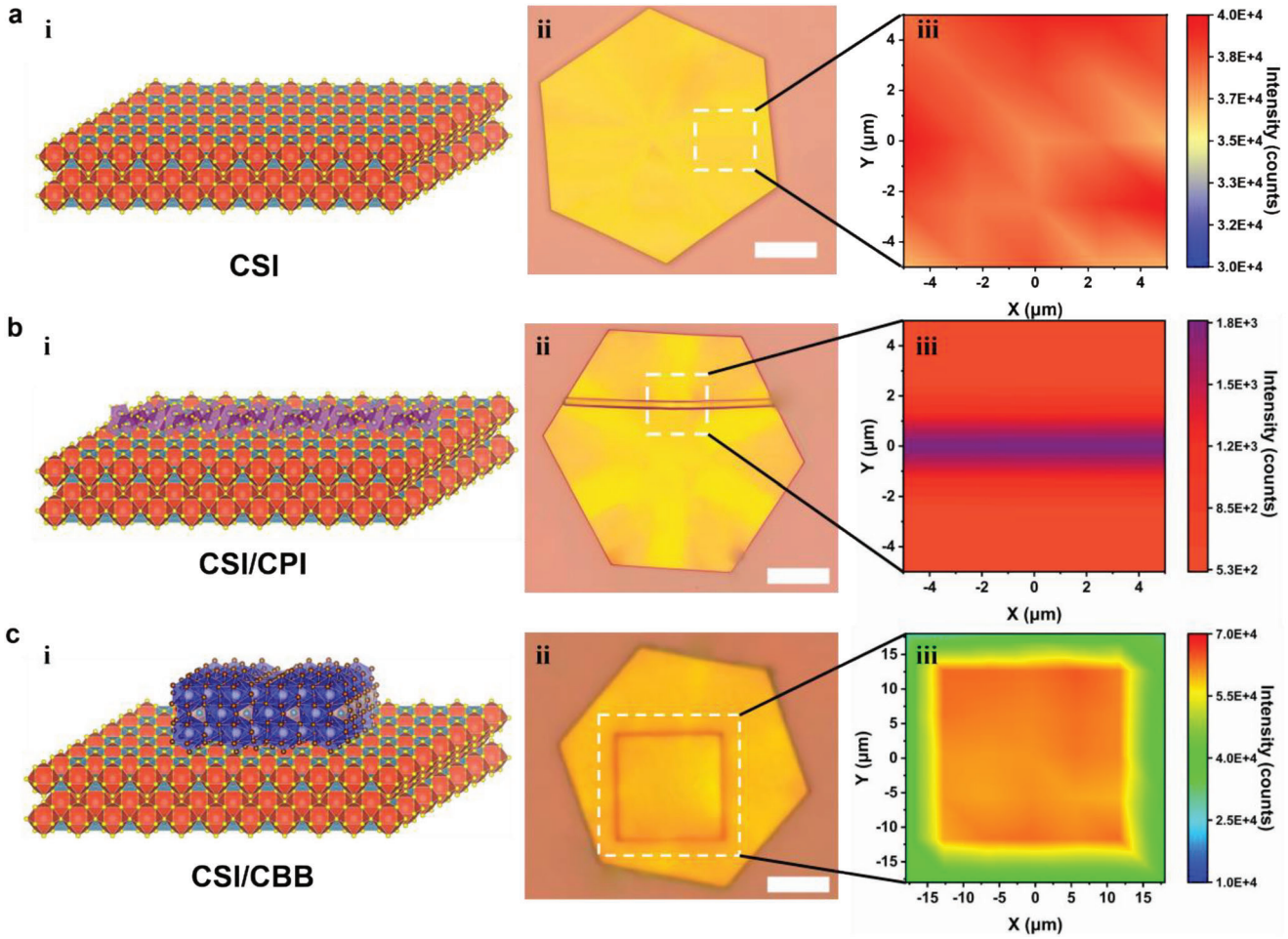

Figure 4. Deterministic fabrication of mixed-dimensional vertical heterostructures based on as-grown AIPSCs. i) Schematics for vertical heterostructures, achieved by gently stacking the crystals of phase 2 to phase 1. ii) Typical optical images of the heterostructures on a clean Si/SiO_2 substrate. iii) PL mappings of the selected area noted by white dash line on corresponding heterostructures (the corresponding wavelengths for mapping signals are 758 nm for CSI, 684 nm for CSI/CPI and 435 nm for CSI/CBB, respectively). a) CSI, serve as bottom support materials. b) CSI/CPI heterostructure. c) CSI/CBB heterostructure.

we tried to fabricate various heterostructures on the basis of as-prepared 2D CSI nanosheets and other kinds of AIPSCs previously synthesized. With the aid of PDMS (polydimethylsiloxane) pick-up transfer technique, desired mixed-dimensional heterostructures are constructed by gently stacking the crystals of phase 2 to phase 1 (for details, see Supporting Information). Utilizing this deterministic fabrication method of arbitrary vertical heterostructures, 2D-1D/2D/3D heterojunctions are both successfully obtained (Figure 4b,c and Figure S5b, Supporting Information). Proved by PL spectroscopy, the PL mapping results in Figure 4 fully verify the integration of CSI/CPI and CSI/CBB, further confirming the success of the heterostructures construction after vertical stacking. This flexible multi-dimensional heterostructures construction process provides a great degree of compositional and structural freedom, allowing us in turn control the electronic structure to achieve customized functionalities, and remains intriguing for further in-depth exploration.

As the CPB AIPSCs have the narrowest PL FWHM with great application potential, we emphatically investigated their optical and optoelectronic properties. The optical properties of CPB are surveyed by UV–vis absorption spectra and PL spectra presented in **Figure 5**a, in which the PL peak shows a red shift to lower energy compared to the absorption edge. CPB exhibits a sharp absorption edge at 538 nm without any shoulder peak, illustrating the phase purity with few impurities. To identify the bandgap value of CPB, fitting processing was conducted with absorption spectra by utilizing Tauc-Plot formula as follows:[37]

$$(\beta h\nu)^{1/n} = B\left(h\nu - E_g\right) \tag{4}$$

where β is extinction coefficient, h is plank constant, ν is frequency, B is a constant term, and E_g is the bandgap of semiconductor materials, n is an index related to the type of semiconductor materials. On account of perovskites this kind of material is direct transition semiconductor, as a result, $n = 0.5$. The fitting curve is shown in the inset of Figure 5a, indicating the bandgap of 2.29 eV, which is similar to previous reports.[38,39] The pure phase of CPB is also confirmed by powder X-ray diffraction (XRD) shown in Figure 5b, in which the experimental result is in good coordination with theoretical calculated profile.

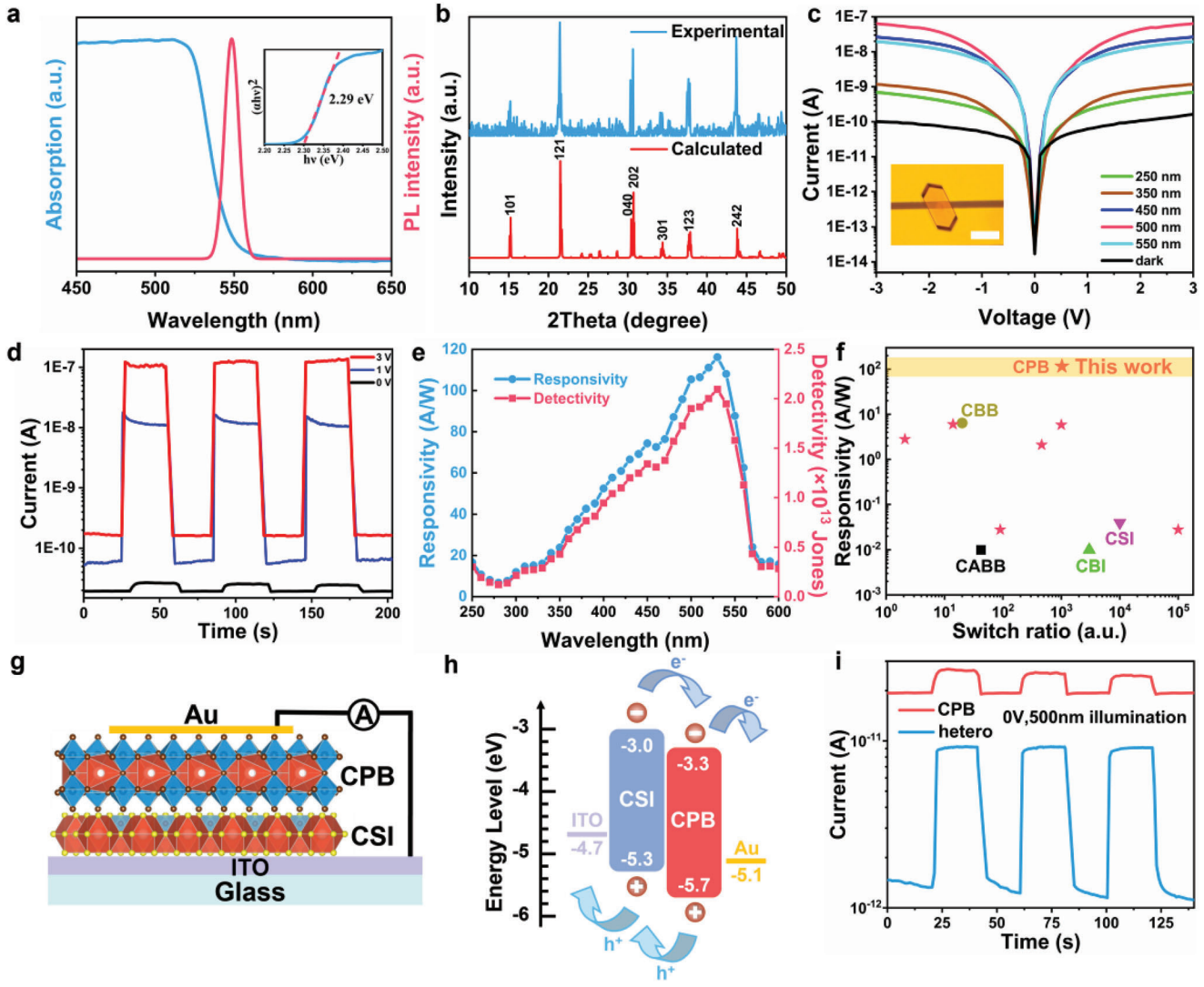

Figure 5. Optical and optoelectronic characterizations of CPB AIPSCs, fabrication of CSI-CPB heterostructure-based PDs and the self-powered performance characterization. a) Optical absorption spectra and PL spectra of CPB (inset: Tauc plot curve). b) Comparison of experimental powder XRD profile and theoretical result calculated from single-crystal diffraction. c) *I–V* curves in the dark and light states (inset: micrograph of the device, scale bar: 30 μm). d) *I–t* curves under 500 nm illumination at the bias of 0, 1, and 3, respectively. e) Responsivity and detectivity as a function of wavelengths at 3 V bias voltage. f) Performance comparison of the AIPSCs-based PDs (pentagram represents CPB). g) Schematic illustration of the device structure of heterojunction-based PDs. h) The energy band alignment diagram of the CSI-CPB heterostructure. i) Self-powered performance comparison between the CPB-based and heterojunction-based PDs.

Specifically, the CPB AIPSCs show very sharp diffraction peaks at 15.2°, 21.5°, 30.6°, 34.3°, 37.7°, and 43.7°, corresponding to (101), (121), (202), (301), (123), and (242) planes of the orthorhombic (*P*nma) crystal structure, respectively.

Having surveyed the optical properties and confirmed the phase purity of CPB AIPSCs, we then characterized their optoelectronic properties by constructing photodetectors (PDs). With the help of PDMS-assisted pick up-release transfer technique (Figure S5a, Supporting Information), parallel CPB-based PDs are fabricated. The current–voltage (*I–V*) curves in dark and light states of the PD device are shown in Figure 5c. The device exhibits an excellent photoresponse characteristic and gains the best photoresponse under 500 nm illumination. The inset shows the planar device architecture of Au-CPB-Au, with the 10 μm gap distance between the two Au electrodes. The current–time (*I–t*) curves under the condition of 500 nm wavelength with 0.24 mW cm^{-2} light power density but different bias voltages are shown in Figure 5d, from which we can see that the device shows boosted photocurrent and low dark current with on/off ratio up to nearly three orders of magnitude. And the device stability is illustrated by performing *I–t* test with 100 cycles at 3 V bias in Figure S7 (Supporting Information). To further compare the responsivity (*R*) and detectivity (*D**) at different wavelengths of the device, we monitored the photoresponse under frequency-adjustable illumination. As shown in Figure 5e, the CPB-based PD exhibits superior performance with *R* up to 120 A W^{-1} and *D** exceeding 2×10^{13} Jones. As shown in Figure 5f and Table S1 (Supporting Information), our as-fabricated CPB-based

device demonstrates better comprehensive photoresponse performance than other AIPSCs-based PDs previously reported. We ascribe the extraordinary performance to the boosted photocurrent and high-quality crystallinity of CPB with few trap-state density. However, the PD device displays a poor photoresponse at 0 V bias voltage, possibly induced by the electrode area difference, illustrating that the self-powered performance has plenty of room for improvement. Thus, we expected to improve it by utilizing the CSI/CPB heterojunctions preciously prepared. The CSI/CPB heterojunction-based PDs construction process is recorded in Figure S5b (Supporting Information) and the device structure is shown in Figure 5g, which adopts a vertical ITO-CSI-CPB-Au architecture. As drawn in Figure 5h, the energy band alignment diagram of CSI-CPB heterojunction illustrates that it belongs to a type-II heterostructure, which is beneficial to the effective separation of electrons and holes and thus improving the detection efficiency.[40] As expected, the self-powered performance of CPB is enhanced by 10 times (Figure 5i). Besides, the CSI/CPB PDs exhibit an obvious rectification characteristic with ratio up to 16, and have faster response times after the heterojunction construction (Figure S6, Supporting Information), further indicating the great potential of these nano-scale heterostructures in the high-performance optoelectronic applications.

3. Conclusion

In summary, this work developed a universal assembly strategy for preparing non-layered AIPSCs at the liquid–air interface, the initial mechanism of this universal long-ranged-ordered assembly behaviors is revealed by applying a new physical growth kinetics model and the classical nucleation theory. The AIPSCs vary a lot in dimension, thickness and morphology, but all of them exhibit high crystallinity, demonstrating the universality of our strategy. In particular, CPI AIPSCs exhibit ultrathin thickness down to 40 nm and CPB AIPSCs obtain ultra-narrow PL FWHM of 11 nm. Based on the as-grown $CsPbBr_3$ AIPSCs, high-performance PDs with ultrahigh responsivity up to 120 A W^{-1} and detectivity exceeding 2×10^{13} Jones are fabricated. Furthermore, mixed-dimensional heterojunctions (2D-1D/2D/3D) construction at the nanoscale are successfully achieved. Impressively, the self-powered performance is further enhanced by this heterojunction fabrication process, suggesting their great potential applications in the highly integrated optoelectronic field.

4. Experimental Section

Interfacial Growth of AIPSCs: Taking the synthesis of CPI as an example, the perovskites precursor solution was prepared by dissolving CsI and PbI_2 (1:1 molar ratio, 0.1 M) into aqueous hydroiodic acid (HI, 55.0–58.0 wt% in H_2O, contains ≤1.5% H_3PO_2) at 110 °C. After 2 h of magnetic stirring, the mother liquid was kept in 70 °C oven. 3–5 µL warm precursor solution was dropped on a clean and hydrophobic substrate, which was then placed on a hot plate of 50 °C in an open ambient environment. Induced by surface tension and solvent volatilization, ultrathin CPI nanobelts appeared at the liquid–air interface and grew larger as time went on. The CBI, CSI, CBB, CPB, and CABB AIPSCs were also synthesized in a similar way. The growth process of AIPSCs was all conducted in an open ambient environment, in which the humidity was generally controlled at about 40% by a dehumidifier.

Materials Characterization: Optical images were captured by Olympus optical microscope. PL spectra and mapping were obtained by Renishaw inVia-Qontor Raman microscope equipped with the excitation wavelength of 532 and 325 nm. The thickness data was measured by step profiler (KLA-Tencor). The crystal structure was characterized by TEM and HRTEM (JEOL2100F). XPS spectra were obtained by X-ray photoelectron spectrometer (PHI5000 VersaprobeIII, Al Kα, energy = 1486.6 eV, voltage = 15 kV, beam current = 4.5 mA). The surface morphology and elements distribution with relative content were confirmed by SEM images and EDS, using field emission scanning electron microscope (Zeiss Sigma 300). UV–vis spectrum of CPB was acquired using a UV–vis spectrometer (Hitachi U-3900H). The composition of CPB was determined by a Bruker D8 Advance X-ray Power diffractometer (XRD, Cu-Kα radiation source, λ = 1.5406 nm).

Device Fabrication and Optoelectronic Measurement: With the help of PDMS pick-up transfer technique, AIPSCs grown at the liquid–air interface could be transferred onto PDMS without any mechanical damage. PDs device fabrication process was completed in a vacuum glove box. Using the accurate transfer platform (Metatest, E1-T), AIPSCs were accurately located in target area with pre-patterned Cr/Au (10/50 nm) electrodes. The Cr/Au electrodes on a clean SiO_2/Si wafer were fabricated by a standard process including photolithography and thermal deposition. For heterojunction-based PDs construction, repeated pick-release procedures were applied. First, AIPSCs of phase 1 carried by PDMS were transferred onto a clean ITO (Indium Tin Oxides) glass, then a second PDMS stamp covered with phase 2 was aligned over a chosen phase 1 nanosheet on the transfer platform. Similarly, top Au electrodes peeled off from evaporated Au films were transferred onto the surface of phase 2 accurately. The whole process requires a high degree of precision. The optoelectronic properties were collected using the semiconductor characterization system (Keithley 4200-SCS) connected a vacuum probe station (Lake Shore) and a 75 W Xe lamp equipped with a monochromator was used as light source. The light density was measured by a NOVA II power meter (OPHIR photonics). All the tests were performed at room temperature.

Supporting Information

Supporting Information is available from the Wiley Online Library or from the author.

Acknowledgements

This work was financially supported by the National Key Research and Development Program of China (No. 2018YFA0703700), the National Natural Science Foundation of China (Nos. 62204047, 92263106, and 12061131009), and the Science and Technology Commission of Shanghai Municipality (Nos. 21520712600 and 19520744300).

Conflict of Interest

The authors declare no conflict of interest.

Data Availability Statement

The data that support the findings of this study are available in the Supporting Information of this article.

Keywords

liquid–air interface, perovskite single crystals, photodetectors

Received: May 21, 2023
Revised: June 28, 2023
Published online:

[1] Y. Liu, Y. Zhang, K. Zhao, Z. Yang, J. Feng, X. Zhang, K. Wang, L. Meng, H. Ye, M. Liu, S. F. Liu, *Adv. Mater.* **2018**, *30*, 1707314.
[2] B. Wenger, P. K. Nayak, X. M. Wen, S. V. Kesava, N. K. Noel, H. J. Snaith, *Nat. Commun.* **2017**, *8*, 590.
[3] Y. Lei, Y. Chen, R. Zhang, Y. Li, Q. Yan, S. Lee, Y. Yu, H. Tsai, W. Choi, K. Wang, Y. Luo, Y. Gu, X. Zheng, C. Wang, C. Wang, H. Hu, Y. Li, B. Qi, M. Lin, Z. Zhang, S. A. Dayeh, M. Pharr, D. P. Fenning, Y. H. Lo, J. Luo, K. Yang, J. Yoo, W. Nie, S. Xu, *Nature* **2020**, *583*, 790.
[4] M. Deng, Z. Q. Li, X. L. Deng, Y. Hu, X. S. Fang, *J. Mater. Sci. Technol.* **2023**, *164*, 150.
[5] Z. Q. Li, Z. L. Li, Z. F. Shi, X. S. Fang, *Adv. Funct. Mater.* **2020**, *30*, 2002634.
[6] J. Liang, X. Han, J. H. Yang, B. Y. Zhang, Q. Y. Fang, J. Zhang, Q. Ai, M. M. Ogle, T. Terlier, A. A. Marti, J. Lou, *Adv. Mater.* **2019**, *31*, 1903448.
[7] K. B. Lin, C. Z. Yan, R. P. Sabatini, W. J. Feng, J. X. Lu, K. K. Liu, D. X. Ma, Y. Y. Shen, Y. P. Zhao, M. L. Li, C. B. Tian, L. Q. Xie, E. H. Sargent, Z. H. Wei, *Adv. Funct. Mater.* **2022**, *32*, 2200350.
[8] Q. Zhang, Q. Y. Shang, R. Su, T. T. H. Do, Q. H. Xiong, *Nano Lett.* **2021**, *21*, 1903.
[9] F. Cao, Z. Q. Li, X. Liu, Z. Shi, X. S. Fang, *Adv. Funct. Mater.* **2022**, *32*, 2206151.
[10] Y. B. Cheng, M. H. Zhu, F. B. Wang, R. C. Bai, J. S. Yao, W. Q. Jie, Y. D. Xu, *J. Mater. Chem.* **2021**, *9*, 27718.
[11] J. Y. Zhang, A. F. Li, B. H. Li, M. M. Yang, X. Hao, L. L. Wu, D. W. Zhao, G. P. Xia, Z. F. Ren, W. B. Tian, D. Y. Yang, J. Q. Zhang, *ACS Photonics* **2022**, *9*, 641.
[12] Z. Q. Li, X. Liu, C. Zuo, W. Yang, X. S. Fang, *Adv. Mater.* **2021**, *33*, 2103010.
[13] F. Yao, J. L. Peng, R. M. Li, W. J. Li, P. B. Gui, B. R. Li, C. Liu, C. Tao, Q. Q. Lin, G. J. Fang, *Nat. Commun.* **2020**, *11*, 1194.
[14] Y. C. Liu, Y. X. Zhang, X. J. Zhu, Z. Yang, W. J. Ke, J. S. Feng, X. D. Ren, K. Zhao, M. Liu, M. G. Kanatzidis, S. Z. Liu, *Sci. Adv.* **2021**, *7*, 8844.
[15] F. B. Wang, R. C. Bai, Q. H. Sun, X. Liu, Y. B. Cheng, S. Z. Xi, B. B. Zhang, M. H. Zhu, S. Q. Jiang, W. Q. Jie, Y. D. Xu, *Chem. Mater.* **2022**, *34*, 3993.
[16] A. G. Ricciardulli, S. Yang, J. H. Smet, M. Saliba, *Nat. Mater.* **2021**, *20*, 1325.
[17] K. Leng, W. Fu, Y. P. Liu, M. Chhowalla, K. P. Loh, *Nat. Rev. Mater.* **2020**, *5*, 482.
[18] J. G. Feng, Y. C. Qiu, L. Jiang, Y. C. Wu, *Adv. Mater.* **2022**, *34*, 2106857.
[19] E. Hong, Z. Q. Li, T. Yan, X. S. Fang, *Nano Lett.* **2022**, *22*, 8662.
[20] L. Y. Li, Y. T. Yu, P. Li, J. X. Liu, L. H. Liang, L. Y. Wang, Y. Ding, X. C. Han, J. M. Ji, S. L. Chen, D. H. Li, P. Liu, S. P. Zhang, M. Q. Zeng, L. Fu, *Adv. Mater.* **2022**, *34*, 2108396.
[21] J. G. Feng, C. Gong, H. F. Gao, W. Wen, Y. J. Gong, X. Y. Jiang, B. Zhang, Y. C. Wu, Y. S. Wu, H. B. Fu, L. Jiang, X. Zhang, *Nat. Electron.* **2018**, *1*, 404.
[22] L. Zhang, J. Jiang, Y. Hu, Z. Lu, X. Wen, S. Pendse, R. Jia, G. C. Wang, T. M. Lu, J. Shi, *J. Am. Chem. Soc.* **2022**, *144*, 17588.
[23] D. X. Pan, Y. P. Fu, N. Spitha, Y. Z. Zhao, C. R. Roy, D. J. Morrow, D. D. Kohler, J. C. Wright, S. Jin, *Nat. Nanotechnol.* **2021**, *16*, 159.
[24] Y. Chen, H. B. Zeng, P. P. Ma, G. Y. Chen, J. Jian, X. Sun, X. M. Li, H. Y. Wang, W. J. Yin, Q. X. Jia, G. F. Zou, *Angew. Chem., Int. Ed.* **2021**, *60*, 2629.
[25] C. K. Lin, Y. Zhang, M. Y. Gao, J. A. Lin, H. K. D. Le, Z. N. Lin, P. D. Yang, *Nano Lett.* **2022**, *22*, 2437.
[26] W. Zheng, X. F. Xiong, R. C. Lin, Z. J. Zhang, C. H. Xu, F. Huang, *ACS Appl. Mater. Interfaces* **2018**, *10*, 1865.
[27] H. Geng, Z. Huang, H. Geng, S. Liu, M. A. Naumova, R. Salvia, S. Chen, J. Wei, L. Zhang, X. Zou, W. Lin, X. Cai, M. Yuan, Z. Hu, X. Shen, R. Yu, K. Zheng, S. E. Canton, X. Fu, *Sci. China Mater.* **2023**, *66*, 2079.
[28] Z. Qi, X. Fu, T. Yang, D. Li, P. Fan, H. Li, F. Jiang, L. Li, Z. Luo, X. Zhuang, A. Pan, *Nano Res.* **2019**, *12*, 1894.
[29] S. K. Shil, F. Wang, Z. X. Lai, Y. Meng, Y. P. Wang, D. X. Zhao, M. K. Hossain, K. O. Egbo, Y. Wang, K. M. Yu, J. C. Ho, *Nano Res.* **2021**, *14*, 4116.
[30] W. C. Pan, H. D. Wu, J. J. Luo, Z. Z. Deng, C. Ge, C. Chen, X. W. Jiang, W. J. Yin, G. D. Niu, L. J. Zhu, L. X. Yin, Y. Zhou, Q. G. Xie, X. X. Ke, M. L. Sui, J. Tang, *Nat. Photonics* **2017**, *11*, 726.
[31] Z. Q. Li, E. L. Hong, X. Y. Zhang, M. Deng, X. S. Fang, *J. Phys. Chem. Lett.* **2022**, *13*, 1215.
[32] L. Canil, T. Cramer, B. Fraboni, D. Ricciarelli, D. Meggiolaro, A. Singh, M. N. Liu, M. Rusu, C. M. Wolff, N. Phung, Q. Wang, D. Neher, T. Unold, P. Vivo, A. Gagliardi, F. De Angelis, A. Abate, *Energy Environ. Sci.* **2021**, *14*, 1429.
[33] X. Deng, Z. Q. Li, F. Cao, E. Hong, X. S. Fang, *Adv. Funct. Mater.* **2023**, *33*, 2213334.
[34] M. Shoaib, X. H. Zhang, X. X. Wang, H. Zhou, T. Xu, X. Wang, X. L. Hu, H. W. Liu, X. P. Fan, W. H. Zheng, T. F. Yang, S. Z. Yang, Q. L. Zhang, X. L. Zhu, L. T. Sun, A. L. Pan, *J. Am. Chem. Soc.* **2017**, *139*, 15592.
[35] I. Cherniukh, G. Raino, T. Stoferle, M. Burian, A. Travesset, D. Naumenko, H. Amenitsch, R. Erni, R. F. Mahrt, M. I. Bodnarchuk, M. V. Kovalenko, *Nature* **2021**, *593*, 535.
[36] R. Frisenda, E. Navarro-Moratalla, P. Gant, D. P. De Lara, P. Jarillo-Herrero, R. V. Gorbachev, A. Castellanos-Gomez, *Chem. Soc. Rev.* **2018**, *47*, 53.
[37] J. H. Tong, Z. N. Song, D. H. Kim, X. H. Chen, C. Chen, A. F. Palmstrom, P. F. Ndione, M. O. Reese, S. P. Dunfield, O. G. Reid, J. Liu, F. Zhang, S. P. Harvey, Z. Li, S. T. Christensen, G. Teeter, D. W. Zhao, M. M. Al-Jassim, M. F. A. M. van Hest, M. C. Beard, S. E. Shaheen, J. J. Berry, Y. F. Yan, K. Zhu, *Science* **2019**, *364*, 475.
[38] J. X. Yu, G. X. Liu, C. M. Chen, Y. Li, M. R. Xu, T. L. Wang, G. Zhao, L. Zhang, *J. Mater. Chem. C* **2020**, *8*, 6326.
[39] M. I. Saidaminov, M. A. Haque, J. Almutlaq, S. Sarmah, X. H. Miao, R. Begum, A. A. Zhumekenov, I. Dursun, N. Cho, B. Murali, O. F. Mohammed, T. Wu, O. M. Bakr, *Adv. Opt. Mater.* **2017**, *5*, 1600704.
[40] X. Y. Zhang, Z. Q. Li, T. T. Yan, L. Su, X. S. Fang, *Small* **2023**, *19*, 2206310.